Materials Science & Engineering A 833 (2022) 142493

Contents lists available at ScienceDirect

Materials Science & Engineering A

journal homepage: www.elsevier.com/locate/msea

The role of the solidification structure on orientation-dependent hardness in stainless steel 316L produced by laser powder bed fusion

Sravya Tekumalla [a,1], Balaji Selvarajou [b,1], Sudharshan Raman [c], Shubo Gao [a], Matteo Seita [a,c,d,*]

[a] School of Mechanical and Aerospace Engineering, Nanyang Technological University, Singapore, 639798, Singapore
[b] Institute of High Performance Computing, Agency for Science, Technology and Research, Singapore, 138632, Singapore
[c] Singapore Centre for 3D Printing, Nanyang Technological University, Singapore, 639798, Singapore
[d] School of Materials Science and Engineering, Nanyang Technological University, Singapore, 639798, Singapore

ARTICLE INFO

Keywords:
Laser powder bed fusion
Stainless steel 316L
Hardness
Anisotropy
Solidification cell structure
Cell spacing along slip direction
Nanoindentation

ABSTRACT

Owing to the rapid cooling rates and directional thermal gradients involved, fusion-based additive manufacturing (AM) processes yield complex, fine solidification structures that impart anisotropic mechanical properties in materials, such as stainless steel 316L (SS316L). In this work, we present a comprehensive study of the mechanical anisotropy of SS316L produced by laser powder bed fusion using instrumented nanoindentation. We produce and test near-single crystal samples oriented along the three principal crystallographic axes—namely ⟨100⟩, ⟨110⟩, and ⟨111⟩—using a Berkovich indenter. We find that the ⟨111⟩ and ⟨100⟩ orientations exhibit the highest and the lowest hardness, respectively. To decouple the contributions of grain orientation and solidification structure to the alloy's mechanical anisotropy, we compare our experimental results against crystal plasticity finite element (CPFE) simulations. We ascribe the hardness anisotropy in SS316L to the cell spacing along the slip direction (CSSD), which is a novel metric that we introduce to account for the role of the solidification structure on plasticity. Our work provides a universal pathway to understanding the microstructure-property relationships in cubic metallic materials that exhibit solidification structures,such as those commonly imparted by fusion-based AM.

1. Introduction

Fusion-based metal additive manufacturing (AM) offers design freedom and versatility in producing intricate engineering components by fusing raw materials together, layer by layer, using a high-energy source [1]. These advantages, however, come at the cost of forming parts with complex, hierarchical microstructures, which include fine solidification structures, site-specific elemental partitioning, and directionally solidified grains with strong crystallographic textures [2,3,68]. This microstructural complexity—which is caused by the highly localized solidification, rapid cooling rates, directional thermal gradients, and cyclic heat-treatments involved in the manufacturing process—imparts non-obvious mechanical anisotropy, even in alloys such as austenitic stainless steel 316L (SS316L) [4–9]. As a result, it is difficult to establish accurate processing-structure-property relationships at the design stage to produce parts with uniform and predictable mechanical response.

One of the challenges in this endeavor is to decouple the effects of crystallographic texture and solidification structure on the mechanical response of alloys and single out the respective contributions. Textures are widely known to have a direct impact on the mechanical anisotropy of SS316L produced by fusion-based AM [5,10]. However, the role of the directionally solidified cellular structures is still elusive. Solidification cells are known to be decorated by a high dislocation density entangled in their walls—which exceeds that found in their interior by one order of magnitude [11]—and a higher concentration of solute—which stems from the solidification of the constitutionally undercooled liquid alloy [2]. Both features hinder glissile dislocation motion [12–14] and thus, enhance the strength of the alloy [15,16]. Owing to the directionality of the cellular structure, it is possible that these additional strengthening mechanisms may have different weights along different crystallographic directions.

In this work, we address this challenge by studying the interplay between solidification structures and crystallographic texture and their

* Corresponding author. School of Mechanical and Aerospace Engineering, Nanyang Technological University, Singapore, 639798, Singapore.
E-mail address: mseita@ntu.edu.sg (M. Seita).
[1] Equal Contribution.

https://doi.org/10.1016/j.msea.2021.142493
Received 9 September 2021; Received in revised form 1 December 2021; Accepted 8 December 2021
Available online 14 December 2021

role on the plastic anisotropy of SS316L produced by laser powder bed fusion (L-PBF). Leveraging on the texture-control capabilities enabled by L-PBF [17], we produce three near-single crystal SS316L cubic samples with strong ⟨011⟩ texture along the build direction (BD ∥ Z-axis) and different crystallographic orientations along the direction perpendicular to BD. These samples are ideal to investigate the orientation- and microstructure-dependent mechanical response of SS316L, as their uniform crystallographic orientation distribution allows separating the contributions of texture and solidification structure on the alloy's mechanical anisotropy. We carry out nanoindentation measurements at room temperature (RT) and combine microscopic observations of the indents on the samples' surface with crystal plasticity finite element (CPFE) simulations to study the local deformation mechanisms at play. Our results elucidate the important role of the solidification structure—consisting of directionally grown cells—on the anisotropic hardening of the three orientations. We explain the plastic anisotropy based on the differences in cell orientation with respect to the active slip systems.

2. Experimental methods

We produced three SS316L cubes (1 cm length each) using a SLM 500 HL (SLM Solutions, Germany) equipped with a 400-Watt IPG fiber laser with a Gaussian beam profile and a spot size of ~ 80 μm. We employed gas atomized powder (Sandvik AB, Sweden) with a nominal composition of Fe–18Cr–14Ni-2.5Mo-0.03C (wt.%) and a particle size distribution between 20 μm and 53 μm. We set the laser power, scan speed, hatch spacing, and layer thickness to 240 W, 600 mm/s, 100 μm, and 40 μm, respectively. To produce samples with near-single crystal orientation, we employed a bi-directional scan strategy and kept the laser scan direction (SD) constant throughout the build [17]. To change the orientation of each of the three samples, we varied the angle between the SD and the X-axis (i.e., the edge of the cube samples) [17]. We used 0°, 55°, and 90° to drive the formation of ⟨100⟩, ⟨111⟩, and ⟨110⟩ orientations along X, respectively as shown in Fig. 1.

We prepared the cube samples using standard metallographic techniques, including grinding up to 800 grit SiC paper and polishing with diamond suspensions of 9 μm, 3 μm and 1 μm diamond sizes, followed by a final polishing using an oxide polishing suspension. We conducted nanoindentation experiments (N = 25) at room temperature (RT) on the polished surfaces of {100}, {110}, and {111} faces of the cubes (parallel to the Y-Z plane) using a Keysight-G200 Nano indenter equipped with a Berkovich tip at a loading rate of 10 mN/s. We measured hardness at a displacement of 800 nm for each orientation according to the Oliver and Pharr method [18,19]. The thermal drift was kept under 0.05 nm/s during each indentation and the samples were unloaded to 10% of the peak load to enable thermal drift correction. To assess the solidification structure, we chemically etched the samples by Kroll's reagent for 30 min. We characterized the solidification structure, grain orientation, and slip trace crystallography by means of field emission scanning electron microscopy (FESEM, JEOL 7800F Prime) and electron backscattered diffraction (EBSD, Symmetry S2 Oxford instruments). We carried out EBSD measurements using a step-size of 0.2 μm for grain orientation mapping and for assessing the local density of geometrically necessary dislocations (GNDs). We performed the analysis of the EBSD data sets using the Channel 5 software (by Oxford Instruments). We classified the grain boundaries based on their local misorientation into low angle grain boundaries (LAGBs) with misorientation ranging between 2° and 15°, and high angle grain boundaries (HAGBs) with a misorientation angle >15°.

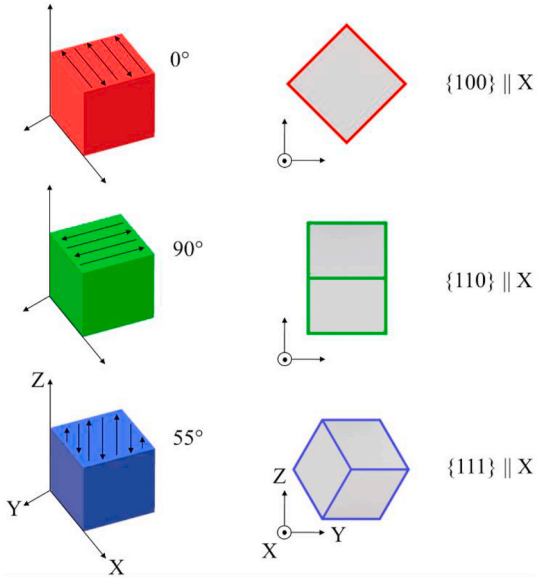

Fig. 1. Schematics of the scan strategy to produce samples with near-single crystal orientation with ⟨100⟩, ⟨111⟩, and ⟨110⟩ orientations along the X axis.

3. Numerical simulation procedure

3.1. Finite element model

We modeled the plastic behavior of ideal single crystals during nanoindentation using three-dimensional (3-D) CPFE simulations (ABAQUS/STANDARD). Fig. 2a shows the 3-D finite element mesh of the substrate and the indenter. We modeled the substrate as a cylindrical block with height and radius of 12 μm each. We discretized the substrate using 28,500 linear hexahedral elements (C3D8 in ABAQUS element library). Based on the recommendation by Giannakopoulos et al. [20], we refined the mesh near the contact area (Fig. 2b), such that the elements are elongated along the direction parallel to the height of the substrate (along the indentation axis) with an aspect ratio greater than 5. These settings are known to minimize errors in the computation of displacements and tractions [20].

We modeled the Berkovich indenter as an isotropic elastic body with a Young's modulus and a Poisson's ratio of 1441 GPa and 0.07, respectively, to mimic a near-rigid solid. We discretized the indenter in 700 linear tetrahedral elements (C3D4 in ABAQUS element library). We set the indenter tip radius to 52 nm, used the penalty method for contact constraint enforcement, and assumed frictionless contact between the indenter and the substrate. We modeled the indentation under quasi-static, isothermal loading conditions in displacement-control mode to match our actual experimental conditions. We prescribed a velocity boundary condition $v = 200$ nm/s to the indenter and limited the time increment to 0.0005 s to ensure convergence. We list the three crystallographic orientations considered in this work in Fig. 2c. Again, we matched the crystallographic directions corresponding to the three indentation axes as well as the lateral directions to those used in the

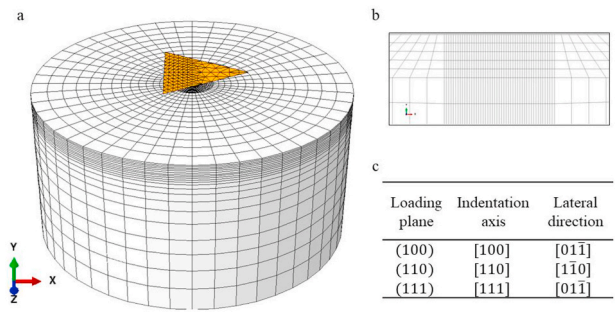

Loading plane	Indentation axis	Lateral direction
(100)	[100]	[01$\bar{1}$]
(110)	[110]	[1$\bar{1}$0]
(111)	[111]	[01$\bar{1}$]

Fig. 2. (a) 3D Finite element mesh of the indented block and the Berkovich indenter, (b) Mesh refinement near the contact area, (c) Orientations of SS316L single crystals considered in this work and their corresponding global coordinate directions along which the crystal orientations are aligned..

experiments.

3.2. Constitutive model

The deformation behavior of the austenitic SS316L substrate is defined by the crystal plasticity constitutive model which describes the constitutive response of single crystal SS316L and accounts for the twelve {111}⟨110⟩ slip systems and the twelve $\{111\}\langle 11\bar{2}\rangle$ twin systems. We report the key constitutive equations in Section 4.3 and provide a detailed description of the CPFE constitutive model in the Appendix.

4. Results

4.1. Nanoindentation experiments

Fig. 3 shows representative high magnification EBSD grain orientation maps and corresponding FESEM images of the {100}, {110}, and {111} surfaces of the cubes, on which we carried out the nanoindentation measurements. Grains in Fig. 3a, e, and i are color-coded according to their orientation along the X-axis, which coincides with the indentation direction. Fig. 3b, f, and j show electron micrographs of the corresponding surfaces after chemical etching. Etching reveals the melt pool boundaries and the solidification structures within the samples, which consist of differently oriented cells. Owing to the strong biaxial texture in the samples, cell orientation is rather consistent throughout the build and fixed to a certain set of directions. In the {100} sample, cells grow parallel to the cube face (i.e., on the Y-Z plane) at an angle of ±45° with respect to the Z-axis [17], as shown in Fig. 3c. Conversely, cells in the {110} sample appear more equiaxed because their growth direction has a component along the X-axis (i.e., out of the plane), as shown in Fig. 3g. Similarly, cells in the {111} sample are slightly elongated since their major axis is inclined at an angle of ∼ 36° with respect to the Z-axis (Fig. 3k).

The experimental nanoindentation load - displacement curves for the three orientations and their corresponding hardness values are shown in Fig. 4a and b, respectively. The curves reveal a substantially higher hardness in L-PBF samples (ranging between 2.5 GPa and 3.1 GPa) compared to conventionally manufactured SS316L (ranging between 1.5 and 2 GPa, depending on the processing history undergone by the material) [21–23]. Similar results showing higher hardness have already been reported by other researchers and were attributed to the presence of the solidification cells in the microstructure, which act as barriers to dislocation motion and promote dislocation entanglement [1,24–26]. We also observe a significant anisotropy in the maximum load (Fig. 4a) and hardness (Fig. 4b) at constant displacement, with the {100} and {111} being the softest and the hardest orientations, respectively. The relative difference in hardness between these two samples is as large as ∼400 MPa. Since we performed indentation away from the melt pool boundaries and in the interior of the grains found in our near-single crystals (see Fig. 3), we expect no contribution from low or high angle grain boundaries, or from solute boundaries [27] to the measured hardness. Further, since our indentation depth is reasonably high (i.e., 800 nm), we also neglect any role of indentation size effects, which is dominant at low indentation depths of <100 nm [28,29], on our measurements. Therefore, we conclude that the hardness anisotropy must be a function of the local crystallographic orientation and the solidification structure imparted by the L-PBF process.

4.2. Slip trace analysis

To shed light on the hardness anisotropy, we analyze the slip band crystallography on each side of the indentation impressions by means of electron microscopy (Fig. 5). By relating the slip trace orientation on the sample surface to the underlying crystal orientation (measured by EBSD), we observe that the traces match the {111} planes across all grain orientations. The unit cell schematics to the right of the SEM images in Fig. 5 illustrate the intersections of {111} planes with the sample surface (dashed lines marking the projection of ⟨110⟩ vectors onto the surface plane), indicating the activation of {111} ⟨110⟩ slip systems in all the three cases. This analysis suggests that dislocation gliding is one of the main deformation mechanisms for nanoindentation compression at room temperature [8,30]. In other words, we observe no activation of unfavorable slip systems in our AM SS316L.

4.3. Crystal plasticity finite element simulations

Since the stress distribution imposed during nanoindentation is complex and typically triaxial—especially when using a Berkovich tip—the plastic behaviour of the alloy as a function of crystallographic orientation cannot be entirely captured by Schmid factor analysis for uniaxial compression. Therefore, we devise a CPFE model to fully

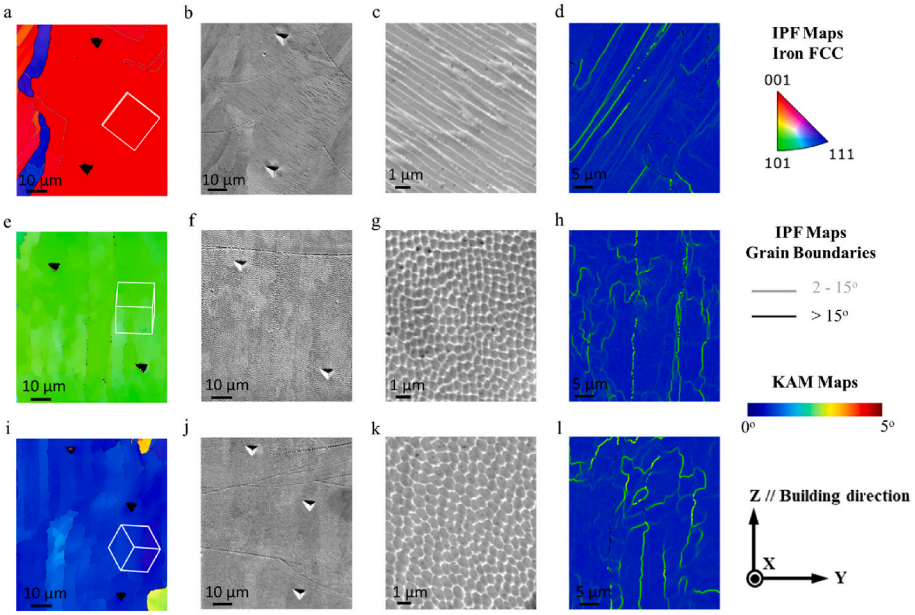

Fig. 3. Grain orientation maps, electron micrographs showing the nano-indented regions in SS316L. (a), (b), (c), (d) correspond to the {100} sample; (e), (f), (g), (h) corresponds to the {110} sample; and (i), (j), (k), (l) correspond to the {111} sample. (a), (e), and (i) are the grain orientation maps, (b), (f), and (j) are the corresponding electron micrographs showing melt pool boundaries, (c), (g), and (k) are the corresponding high magnification electron micrographs showing the solidification cell structures on the sample surfaces, and (d), (h), (l) are the corresponding KAM maps computed from the raw EBSD data plotting the average misorientation between every pixel and a kernel of surrounding pixels.

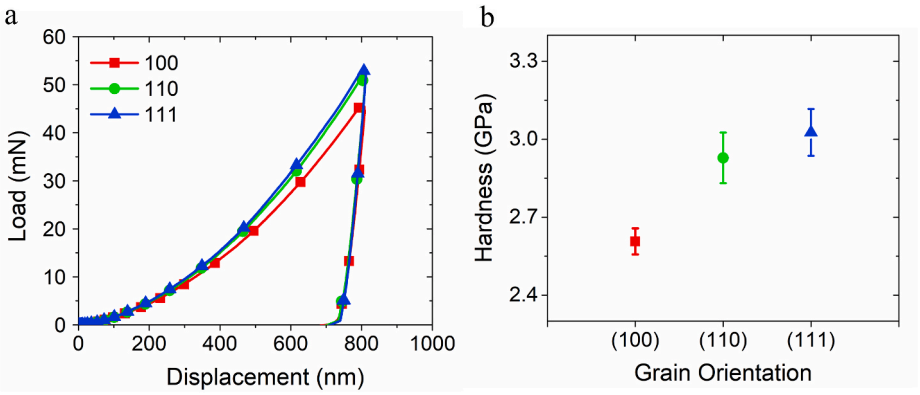

Fig. 4. (a) Load-displacement curves from loading to unloading stage (unloaded at a maximum displacement of 800 nm), (b) Experimentally measured hardness for the {100}, {110}, and {111} samples.

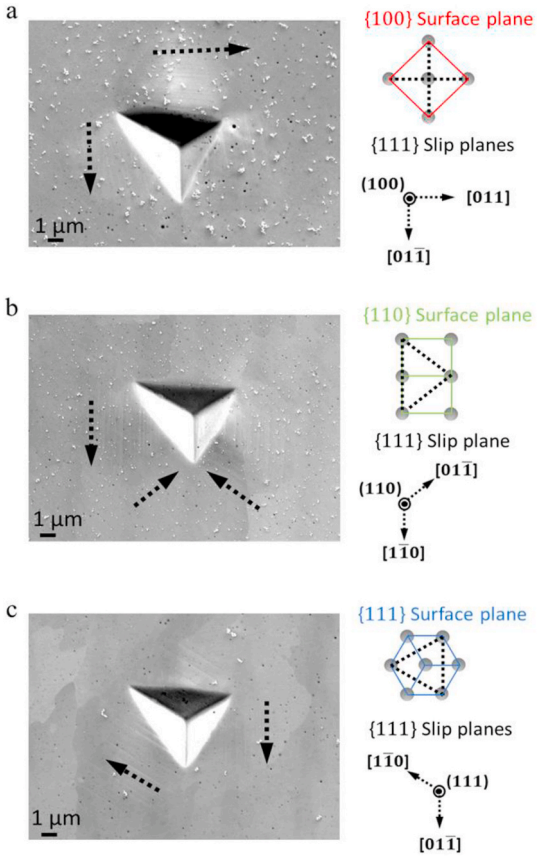

Fig. 5. Electron micrographs of slip traces around the indents on the (a) {100}, (b) {110}, and (c) {111} sample surfaces.

resolve the stress state imposed by the indenter and study the plastic response of the L-PBF SS316L. In our model, we describe the initial strength of the slip systems using the Taylor relation:

$$g_0 = g_f + \nabla \mu b \sqrt{\rho_{GND} + \rho_{SSD}} \tag{1}$$

The first term in the equation, g_f, represents the cumulative strength of the slip system due to lattice friction, solid solution strengthening, and precipitation strengthening. The second term in Eq. (1) represents the strengthening contribution coming from dislocation interactions on the activated slip systems. Here, μ is the shear modulus of the material, $b = \frac{a_0}{\sqrt{2}}$ is the magnitude of the Burgers vector of the slip system (with lattice constant a_0), and ∇ is an empirical constant with a value of 0.33 for a uniform distribution of dislocations [31]. ρ_{SSD} and ρ_{GND} refer to the density of the statistically stored dislocations and GNDs, respectively. Their sum equals the total dislocation density, ρ_{TOT}. It is noteworthy that we do not take into account the contribution of grain boundary strengthening to the slip systems strength since our samples are all single crystal-like.

To estimate the above variables and validate our model, we use the experimental results published by Karaman et al. [32] on the tensile behavior of single crystal-like AISI SS316L along three different crystallographic directions, viz. [100], [123], and [111]. We set $g_f = 95$ MPa, and $\rho_{TOT} = 1 \times 10^{12} \mathrm{m}^{-2}$ (which is typical for annealed alloys). We take the elastic constants from previously published literature and estimate the remaining parameters by fitting the model to the data provided by Karaman et al. [32]. Because deformation twinning is known to be an active deformation mechanism in certain crystallographic orientations and is a function of the loading/stress state [5,8,33], we include slip-twin and twin-slip interactions in our CPFE model by computing the orientation-dependent stacking fault energy (SFE) of the material [32–35]. In the Appendix, we report the detailed description of all the constitutive equations for slip and twinning as well as all the variables which we use in the model (in Table A-2), alongside the corresponding sources. Fig. 6 compares the simulated stress-strain response of the single crystals along different crystallographic axes with the experimental results by Karaman et al. [32]. The good match between simulations and experiments suggests that the model quantitatively captures the plastic behavior of conventionally manufactured SS316L.

It is widely accepted that fusion-based AM processes enhance the strength of SS316L as a result of the complex microstructure consisting of fine solidification structures and a higher initial dislocation density

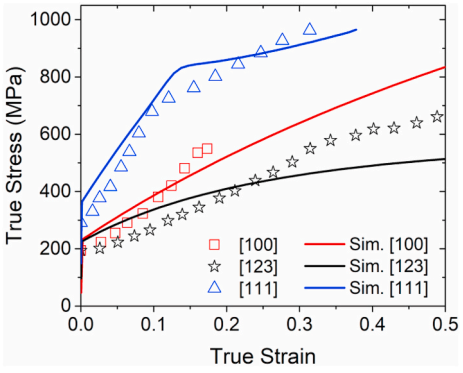

Fig. 6. Stress-strain response of single crystalline SS316L produced under tensile loading along different orientations; the symbols are the experimental results of Karaman et al. [32] and the solid lines are the predictions with the current model.

[36]. Thus, to adapt our model to L-PBF SS316L, we set the initial dislocation density to the experimentally measured values in our as-produced samples without modifying any other parameters. To estimate the new GND density, we compute the kernel average misorientation (KAM) maps corresponding to the raw EBSD data shown in Fig. 3d, h, and l and use the empirical relationship $\rho_{GND} = \frac{\lambda\theta}{Xb}$ [37]; where $\lambda = 2$ (for low angle tilt boundaries), θ corresponds to the local misorientation angle, X is the step-size used to acquire the EBSD measurements, and b is the magnitude of Burgers vector. The resulting average GND density in all three samples is $\sim 1 \times 10^{14}$ m^{-2}, which is in line with what has been previously reported for L-PBF SS316L [11,38]. Based on the work by Cui et al. [39], we estimate the SSD density in our samples to be roughly one order of magnitude lower than that of GNDs. Therefore, we compute an updated $\rho_{TOT} = 1.1 \times 10^{14}$ m^{-2} for the SS316L samples in this work.

To ascertain the role of this higher dislocation density on the hardness anisotropy, we compare the CPFE simulations using a total initial dislocation density of 1×10^{12} m^{-2} and 1.1×10^{14} m^{-2}. We plot the simulation results in Fig. 7, including the load – displacement curves and hardness values, alongside the experimentally measured ones. To quantify the hardness anisotropy, we define a normalized hardness value, $\eta_{hkl} = \frac{H_{hkl}}{H_{100}} - 1$; where H_{hkl} and H_{100} are the hardness values on the $\{hkl\}$ and $\{100\}$ planes, respectively. The CPFE predictions on the alloy hardness are significantly lower compared to what we measure experimentally, regardless of the ρ_{TOT} value used. The results from simulations with $\rho_{TOT} = 1 \times 10^{12}$ m^{-2} are not surprising since conventional SS316L has similar hardness and is known to exhibit isotropic mechanical properties [8,9]. However, for the case with $\rho_{TOT} = 1.1 \times 10^{14}$ m^{-2}, we only find marginal anisotropy (i.e., $\eta_{\{110\}} = 0.05.\eta_{\{111\}} = 0.05$). While this result indicates that the initial dislocation density plays a role on plastic anisotropy, it does not entirely capture the marked hardness anisotropy seen from our nanoindentation measurements (Fig. 7b), which yields $\eta_{\{110\}} = 0.12$ and $\eta_{\{111\}} = 0.16$. These results indicate that plain slip, deformation twinning, and initial dislocation density, do not play a major role on the orientation-dependent anisotropy observed. Since grain orientation has no direct effect on the hardness anisotropy, we attribute the discrepancy between CPFE simulations and nanoindentation measurements to the solidification cell structure in L-PBF SS316L.

4.4. Microstructure analysis

A visual comparison between the slip trace analysis in Fig. 5 and the solidification cell structures in Fig. 3 suggests that the activated dislocations in different samples may intersect solidification cells at different angles, even though they move along the same nominal crystallographic direction. The reason for these differences stems from the preferential orientation of solidification cells during L-PBF, which grow along the ⟨100⟩ crystal axes [3]. Therefore, while the slip directions across all 12 slip systems are symmetrically equivalent, the number of cells that dislocations intersect along different slip directions is not necessarily identical. We illustrate this concept in the schematics shown in Fig. 8a.

Since the solidification cell walls are decorated with solute elements—such as chromium and molybdenum in SS316L—and copious dislocations—which originate from the rapid solidification of the alloy—they provide additional resistance to dislocation motion and thus, increase hardness [2]. Several works have correlated the average cell size in bulk samples with hardness and strength using the Hall-Petch relationship [25,40]. While this metric may be suitable to model hardening in polycrystals with random cell orientation distribution, it fails at capturing the nuanced differences in individual grain orientations, where the distance between cell walls along the slip directions may differ depending on the local crystallographic orientation and loading axis. Thus, we propose the *cell spacing along the slip direction* (CSSD) as a more accurate metric to account for hardening from cell structures. The higher the density of cell walls along the slip direction (i.e., the smaller CSSD), the higher the hardening effect; in a similar fashion to the grain boundary strengthening predicted by the Hall-Petch relationship [41]. We measure the CSSD by identifying the activated slip systems, computing the slip plane tilt with respect to the growth direction of solidification cells, and deducing the distance between cell boundaries onto such a plane along the slip direction using trigonometry. Fig. 8a shows a visual representation of the 3-D cell structure and the differences in CSSD along two different slip directions $[01\bar{1}]$ and $[1\bar{1}0]$, represented by orange and purple arrows, respectively.

To ascertain the role of CSSD on hardness anisotropy, we include the strengthening mechanism arising from cell boundaries in the strength of the slip systems in the CPFE simulations. To this end, we modify Eq. (1) to distinguish between strengthening effects caused by SSDs—which are uniformly distributed within solidification cells—and the Hall-Petch type of strengthening mechanism caused by the cell walls—which arises from the localization of GNDs and segregated solute elements. The updated equation describing the slip system strength becomes:

$$g_0 = g_f^{AM} + \nabla^{\mathrm{AM}} \mu b \sqrt{\rho_{SSD}} + \frac{k_{HP}}{\sqrt{\mathscr{D}}} \tag{2}$$

Here, g_f^{AM} represents the strengthening of the slip system in L-PBF SS316L, the dislocation strengthening term accounts for only SSDs, and the third term $\frac{k_{HP}}{\sqrt{\mathscr{D}}}$, includes the Hall-Petch strengthening contribution of GNDs. Although g_f^{AM} in Eq. (2) corresponds to the same physical quantity as g_f in Eq. (1), its value (40 MPa [39]) is smaller than the value of g_f (95 MPa) [42]. This difference can be rationalized by the fact that

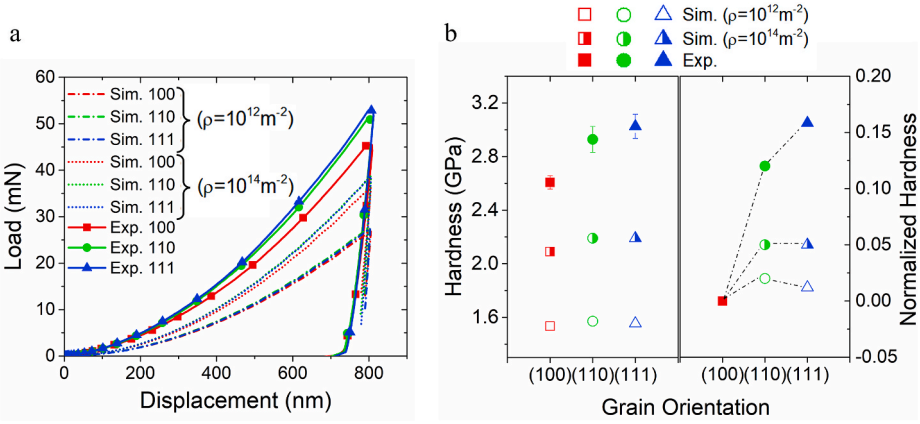

Fig. 7. (a) Simulated load-displacement curves at dislocation densities of 10^{12} m^{-2} and 10^{14} m^{-2} in comparison to the experimental ones, (b) Simulated and experimentally measured hardness and normalized hardness for {100}, {110}, and {111} samples.

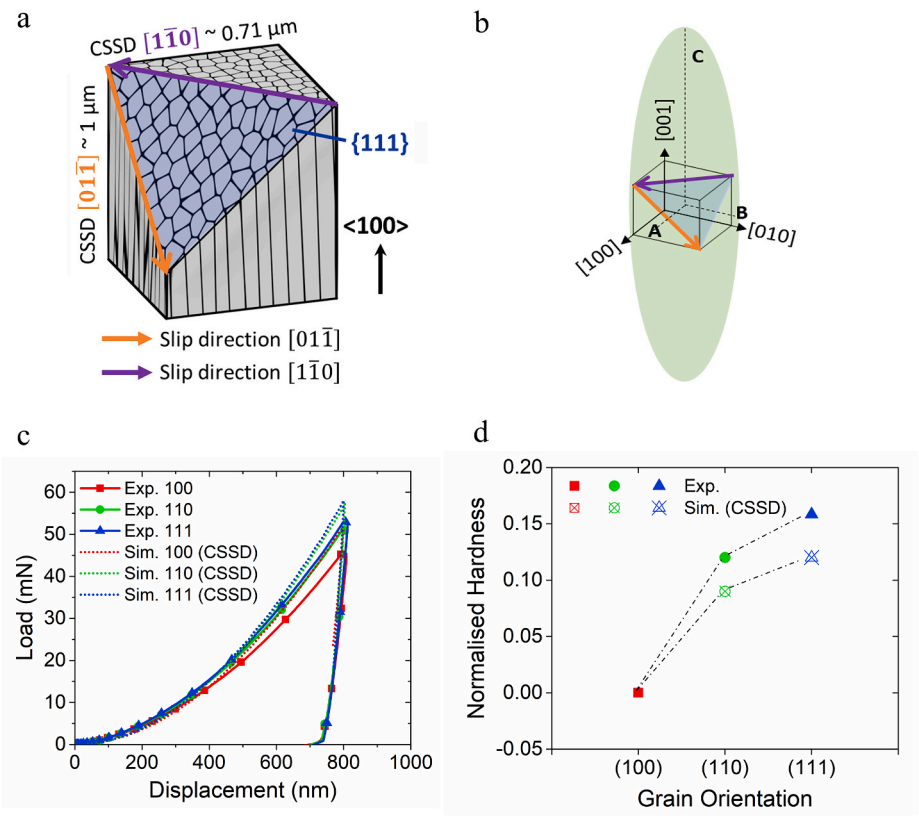

Fig. 8. (a) 3D visual representation of cell structures, slip directions, and cell spacing along slip direction (CSSD) values for two different slip directions. (b) Schematic showing the crystal embedded in an ellipsoid of semi-axes lengths A, B, and C. For zone axis along [001] and C >> A = B as in the case of sub-grain cells, the four slip systems which are normal to the major axis of the ellipsoid have CSSD equal to 2A whereas the other eight slip systems have CSSD of $\sim 2\sqrt{2}$ A. The former and latter are shown as orange and purple vectors; (c) Comparison of load-displacement curves obtained from the experiments and simulations, (d) Comparison of the normalized hardness values obtained from the experiments and simulations at peak load. With CSSD and without CSSD refer to the simulations wherein the strengthening effect of the CSSD is considered and ignored, respectively. (For interpretation of the references to color in this figure legend, the reader is referred to the Web version of this article.)

segregation of solute elements to the cell walls leads to an overall reduction in solute strengthening. Further, we take the empirical constant ∇^{AM} to be 0.23 for a distribution of dislocations that forms substructures within grains [43]. In the Hall-Petch strengthening term, k_{HP} is the Hall-Petch parameter and $\mathscr{D}$ is the length scale corresponding to the microstructural interfaces hindering dislocation motion. In a typical polycrystal, Hall-Petch strengthening comes from the presence of grain boundaries. If grains are equiaxed, a single value of $\mathscr{D}$ equal to the average grain diameter may be used to predict the strength of all slip systems. In the present case of a L-PBF single crystal, however, segregation cell walls act as additional barriers to dislocation motion. Since these cells have high aspect ratio, $\mathscr{D}$ will be different in different slip systems [16]. Thus, we set $\mathscr{D}^{\alpha} = CSSD^{\alpha}$ for each activated slip system α, and calculate it as the chord length of a vector passing through the center of the cell along the Burgers direction. To ease the computation, we approximate a cell to an ellipsoid with the major axis oriented along the ⟨100⟩ direction (see Fig. 8b). Considering a local coordinate system $\bar{x}\bar{y}\bar{z}$ with respect to the axes of the ellipsoidal cell ($\bar{z}$ being aligned to its major axis), we define the resulting CSSD for each slip system, α, as [44]:

$$CSSD^{\alpha} = \frac{2}{\sqrt{\left(\frac{b_{\bar{x}}{}^{\alpha}}{A}\right)^2 + \left(\frac{b_{\bar{y}}{}^{\alpha}}{B}\right)^2 + \left(\frac{b_{\bar{z}}{}^{\alpha}}{C}\right)^2}} \tag{3}$$

Here, $A \sim 350\ nm$, $B \sim 350\ nm$, and $C \sim 7.2\ \mu$ m are the semi-axis lengths of the ellipsoidal cell measured from solidification cell structures shown in Fig. 3. $b_{\bar{x}}$, $b_{\bar{y}}$, and $b_{\bar{z}}$ are the components of the unit Burgers vector in the local $\bar{x}\bar{y}\bar{z}$ coordinate system. In the case of a ⟨100⟩ zone axis and $C >> A = B$ (as it is for solidification cells), the four slip systems whose slip directions are normal to the ellipsoid major axis have CSSD equal to $2A \sim 710\ nm$, whereas the other eight have CSSD of $= 2\sqrt{2}A \sim 1000\ nm$. These values are in good agreement with those obtained via slip trace analysis and are shown in Fig. 8a.

Knowing the orientation of the solidification cells in our SS316L cube samples, we use Eq. (3) to calculate the CSSD for each slip system and feed it to the Hall-Petch strengthening model in the CPFE simulations. While we do not directly account for the role of cell spacing in the definition of the strength of the twin systems, we note that the model implicitly takes it into account since the activation of multiple slip systems is a prerequisite for the activation of twinning [45].

Fig. 8c and d shows the updated load – displacement curves and normalized hardness values after considering the CSSD effects in our CPFE simulations. The new curves closely mirror the experimental ones for all the three orientations and evince a significant anisotropy with $\eta_{\{110\}} = 0.09$ and $\eta_{\{111\}} = 0.12$. Therefore, we conclude that the measured mechanical anisotropy arises from the differences in CSSD in the three orientations.

5. Discussion

To rationalize the differences in hardness in the three samples, we analyze the CSSD within the plastic region below the indents from CPFE simulations, as shown in Fig. 9. We note that the plastic deformation in {110} is predominantly accommodated by slip systems with lower CSSD values of 710 nm. By contrast, the {100} orientation predominantly deforms by slip systems with higher CSSD values of 1000 nm. Therefore, owing to its lower CSSD values, the hardness of {110} is higher than that of {100}. In the case of {111}, the simulations show that the slip systems with a lower CSSD value are activated to accommodate deformation beneath the indenter (see the black arrow in Fig. 9c). This argument is supported by the experimental slip trace analysis shown in Fig. 5, which evinces activation of multiple slip systems with lower CSSD values in the cases of {110} and {111}. We therefore conclude that the activation of slip systems with lower CSSD values leads to a larger increase in hardness in {110} and {111} compared to {100}.

Although the trend in hardness that we observe in our CPFE simulations (see Fig. 8d) is a close qualitative match with what we find in our experimental results, some quantitative discrepancies still exist. There

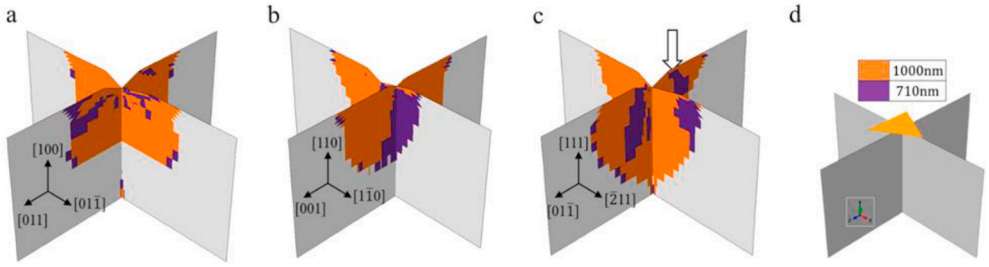

Fig. 9. Contours of the CSSD of the most active slip systems on two cross sections of the substrate for indentation on the (a) {100}, (b) {110}, (c) {111} planes, (d) orientation of the cross-sectional planes with respect to the indenter.

are several possible reasons that could explain this mismatch. For instance, while we ensured to measure hardness at a higher depth of 800 nm to mitigate the effect of strain gradients on the hardness anisotropy, our simulations do not include the role of strain gradient plasticity, which may affect the local strain distribution within the alloy, and therefore, the load applied in the simulations [46]. The primary reason for the discrepancy may be due to our choice to use the Hall-Petch relationship to correlate CSSD with slip system strength. Since no study has proposed a Hall-Petch coefficient specific to cell-walls strengthening to date, we select a coefficient of 16.5 MPa $\sqrt{\text{mm}}$, which equals the product of that associated with the slip system strength (taken to be 5.5 MPa $\sqrt{\text{mm}}$) and an average Taylor factor of ~3 [39]. This value is approximately equal to the Hall-Petch coefficient used for coarse-grained microstructures, and thus deemed appropriate for our single crystal-like samples. However, we note that the high cell-walls density in our material (as confirmed by average CSSD values ≤ 1 μm) could call for a larger Hall-Petch coefficient, which is typical of fine-grained microstructures (e.g., of the order of ~50 MPa $\sqrt{\text{mm}}$ in stainless steels [47]). It may be noted that a larger Hall-Petch coefficient would increase the difference in strength between the slip systems with different CSSD values, which would in turn increase the hardness anisotropy. With regards to the Hall-Petch exponent, the existing literature is inconclusive on what exponent to employ in steels. Some have argued that the value should scale with the applied strain [48]. Others [49] have shown that the sub-grain structures forming as a result of plastic deformation may call for smaller exponent (approximately −1). Here, we employ the conventional value of −0.5. Clearly, the choice of the Hall-Petch parameters affects the magnitude of the hardness anisotropy in our experiments. We select conservative values for both the coefficient and exponent not to overestimate CSSD strengthening in SS316L (and thus the resulting hardness anisotropy). Indeed, several works have proposed other analytical expressions to link strength to the size of dislocation substructures, which yield more significant contributions. Gahn et al. [50], for instance, showed that the strengthening effect due to the internal stresses caused by the compositional variations between cell interiors and cell walls may be estimated by:

$$g^{cell\ walls} = c_1 \left(\frac{\mu b}{\mathscr{D}}\right)^{\frac{2}{3}} \tag{4}$$

Here $g^{cell\ walls}$ is the contribution to the strength from the cell walls. Using Eq. (4), Smith et al. [15] calculated $c_1 = 27.7MPa^{1/3}$ as the result of Cr segregation to cell walls in stainless steel 304L. By applying Eq. (4) to our results, we find the difference in strength between slip systems with CSSD values of 710 nm and 1000 nm to be ~52 MPa, which is ~1.5 times the difference between the strength of the slip systems obtained using the Hall-Petch relationship in our work. In another work, Staker et al. [51] proposed a different relationship between dislocation substructures and yield strength given by:

$$g^{substructures} = c_2 \frac{\mu b}{\mathscr{D}} \tag{5}$$

Here, c_2 is a non-dimensional constant determined to be 10.5 for dislocation structures in a number of FCC materials, such as copper and aluminum [51]. Using Eq. (5) and assuming the same c_2 value for simplicity, we find the difference between the strength of the slip systems with CSSD values of 710 nm and 1000 nm to be ~85 MPa, which is ~2.5 times higher than what we report in this work through the Hall-Petch relationship. Either approaches—using Eq. (4) or Eq. (5)—would therefore increase the hardness anisotropy estimates for our alloy.

In view of the above and due to the current uncertainty around what relationship to use to estimate the strengthening contribution coming from dislocation substructures in L-PBF steels, we have chosen to rely on Hall-Petch relationship and to use parameters that, we believe, best represent the dislocation cells found in our samples. Indeed, Fig. 8c shows a good match between the experimentally measured load-displacement curves and those computed through our simulations, indicating that the parameters we chose are a good fit to represent dislocation cells. It is noteworthy that the key role of CSSD on the plastic anisotropy in L-PBF SS136L is clear from this work, despite the uncertainty in the selection of the strengthening relationship and fitting parameters.

Our results provide direct evidence that the solidification structure underpins the plastic anisotropy of L-PBF SS316L, which varies in non-obvious ways as a function of crystal orientation. These conclusions are in line with the work by Voisin et al. [16], who recently noted that a single microstructural length scale cannot be used to characterize the strengthening mechanisms at play in the complex microstructures that form during fusion-based AM processes; especially given the important role of segregation cell structures. Our CSSD metric could provide new insights and opportunities into understanding the strengthening mechanism at play in a wide range of alloy systems produced by fusion-based AM processes. We speculate that the CSSD effect may be even more pronounced in alloys exhibiting nano-precipitates or inclusions at cell boundaries [52]. If controlled—for instance by varying the cell size [38] and solidification texture [17] via AM process parameter tuning—this plastic anisotropy could also provide new avenues for tailoring the mechanical behavior of structural materials to an unprecedent level of detail.

6. Conclusions

In this work, we provide new insights into the role of the solidification structure on the mechanical anisotropy of L-PBF SS316L by testing near-single crystalline specimens using instrumented nanoindentation and modeling their plastic behavior by means of crystal plasticity finite element (CPFE) simulations. The main findings of our work are:

1. Nanoindentation experiments on L-PBF SS316L reveal a measurable hardness anisotropy with ⟨111⟩ orientation exhibiting the highest and ⟨100⟩ exhibiting the lowest value.
2. We ascribe the anisotropy to the cell spacing along slip direction (CSSD), which quantifies the linear density of solidification cell

boundaries on the activated slip system. Indeed, hardness scales inversely to CSSD, following the Hall-Petch relationship.
3. To corroborate our hypothesis, we run CPFE simulations that include the CSSD contribution to the alloy plastic behavior and demonstrate their key role on the orientation-dependent plasticity of the alloy. By contrast, we find that deformation slip, twinning, initial dislocation density, and grain orientation do not impart significant mechanical anisotropy.

These findings carry important implications for designing and understanding the behavior of metal alloys produced by fusion-based AM processes. They enable more accurate prediction of the mechanical behavior—and possible anisotropy—parts in service produced by fusion-based AM. Moreover, they provide new insights into the complex strengthening mechanisms at play not just in SS316L, but also in a wide range of other alloy systems produced by means of fusion-based AM processes.

Credit authorship contribution statement

Sravya Tekumalla: Conceptualization, Methodology, Investigation, Validation, Formal analysis, Writing – original draft; **Balaji Sevarajou:** Simulations, Validation, Writing – original draft; **Sudharshan Raman:** Methodology, **Gao Shubo:** Methodology; **Matteo Seita:** Conceptualization, Supervision, Funding acquisition, Writing- Reviewing and Editing.

Data availability

The raw/processed data required to reproduce these findings cannot be shared at this time as the data also forms part of an ongoing study.

Declaration of competing interest

The authors declare that they have no known competing financial interests or personal relationships that could have appeared to influence the work reported in this paper.

Acknowledgments

The authors would like to acknowledge Mallory Wittwer for his assistance with 3D rendering. This work was supported by the NTU Presidential Postdoctoral Fellowship (Grant number: 04INS000761C160), National Research Foundation (NRF) Singapore, under the NRF Fellowship program (NRF-NRFF2018-05), and A*STAR, Singapore under the Structural Metals and Alloys Program (Grant number: A18B1b0061). Access to shared experimental facilities used in this work was provided by the School of Mechanical and Aerospace Engineering and the Facility for Analysis Characterization Testing and Simulation at NTU.

Appendix

A. Crystal plasticity constitutive model

The CPFE model describes the constitutive response of a perfect single crystal of SS316L and accounts for twelve $\{111\}\langle 110\rangle$ slip systems and twelve $\{111\}\langle 11\bar{2}\rangle$ twin systems based on the framework developed by Refs. [53–55]. Both slip and twinning occur in the close packed $\{111\}$ planes. The Burgers vector of the former and latter are $\frac{1}{\sqrt{2}}\langle 110\rangle$ and $\frac{1}{6}\langle 11\bar{2}\rangle$, respectively, with the latter being the leading Shockley partial of the former. Table A-1 lists the twelve slip systems and the partials corresponding to each slip system.

Table A-1
Slip plane normals (Column 1) and slip directions (Column 2) in FCC austenitic S316L. The partials whose sum forms the slip directions are shown in Columns 3 and 4. The Burgers vector of the twin systems are given by the leading Shockley partials of the slip systems.

Slip/twin plane	Slip direction	Partial 1	Partial 2
(111)	$[01\bar{1}]$	$[1\bar{1}\,2]$	$[\bar{1}\,2\bar{1}]$
(111)	$[\bar{1}\,01]$	$[\bar{2}\,11]$	$[\bar{1}\,\bar{1}\,2]$
(111)	$[1\bar{1}\,0]$	$[12\bar{1}]$	$[2\bar{1}\,\bar{1}]$
$(\bar{1}\,\bar{1}\,1)$	$[01\bar{1}]$	$[12\bar{1}]$	$[\bar{1}\,12]$
$(\bar{1}\,\bar{1}\,1)$	$[101]$	$[1\bar{1}\,2]$	$[211]$
$(\bar{1}\,\bar{1}\,1)$	$[\bar{1}\,\bar{1}\,0]$	$[\bar{2}\,\bar{1}\,\bar{1}]$	$[\bar{1}\,\bar{2}\,1]$
$(1\bar{1}\,1)$	$[011]$	$[\bar{1}\,21]$	$[112]$
$(1\bar{1}\,1)$	$[1\bar{1}\,0]$	$[2\bar{1}\,1]$	$[12\bar{1}]$
$(1\bar{1}\,1)$	$[\bar{1}\,01]$	$[\bar{1}\,\bar{1}\,2]$	$[\bar{2}\,1\bar{1}]$
$(\bar{1}\,11)$	$[01\bar{1}]$	$[\bar{1}\,2\bar{1}]$	$[1\bar{1}\,2]$
$(\bar{1}\,11)$	$[\bar{1}\,01]$	$[\bar{1}\,12]$	$[\bar{2}\,\bar{1}\,1]$
$(\bar{1}\,11)$	$[110]$	$[21\bar{1}]$	$[121]$

The total deformation gradient $\mathbf{F}$ is the product of the elastic $\mathbf{F^e}$ and plastic $\mathbf{F^p}$ parts [56]:

$$\mathbf{F} = \mathbf{F^e F^p} \tag{A-1}$$

From the initial reference configuration, $\mathbf{F^p}$ transforms the material to a stress-free intermediate configuration and $\mathbf{F^e}$ transforms the material from the intermediate configuration to the final configuration through lattice stretching and rotation. Using Eq. A-1, the elastic and plastic parts of the velocity gradient are obtained as

$$\underbrace{\mathbf{F} = \mathbf{F^e F^{e-1}}}_{\mathbf{L^e}} + \underbrace{\mathbf{F^e F^p F^{p-1} F^{e-1}}}_{\mathbf{L^p}} \tag{A-2}$$

where $\mathbf{L}^e$ and $\mathbf{L}^p$ are the elastic and plastic parts of the velocity gradient respectively in the current configuration. After Kalidindi et al. [55], $\mathbf{L}^p$ can be written as:

$$\mathbf{L}^p = \underbrace{\left(1 - \sum_{\beta=1}^{N_{tw}} f^\beta\right) \sum_{\alpha=1}^{N_{sl}} \dot{\gamma}^\alpha (s^\alpha \otimes n^\alpha)}_{\text{Slip in matrix}} + \underbrace{\sum_{\beta=1}^{N_{tw}} \dot{\gamma}^\beta (s^\beta \otimes n^\beta)}_{\text{Twin in matrix}} + \underbrace{\left(\sum_{\beta=1}^{N_{tw}} f^\beta\right) \sum_{\alpha'=1}^{N_{sl}} \dot{\gamma}^{\alpha'} (s^{\alpha'} \otimes n^{\alpha'})}_{\text{Slip in twin}} \tag{A-3}$$

Here, α and β are the slip and twin systems, respectively, α' is the slip inside the twinned regions, f^β is the volume fraction (v.f.) of the β^{th} twin system, and $N_{sl} = 12$ and $N_{tw} = 12$ are the number of slip and twin systems, respectively. For the i^{th} slip/twin system, s^i and n^i are the slip/twin direction and slip/twin plane normal, respectively, and $\dot{\gamma}^i$ is the shear rate.

A.1 Constitutive equations for slip

We employ a viscoplastic power law to model plastic slip [57]:

$$\dot{\gamma}^\alpha = \dot{\gamma}_0^\alpha \left|\frac{\tau^\alpha}{g^\alpha}\right|^{m_{sl}} \operatorname{sgn}(\tau^\alpha) \tag{A-4}$$

Here, $\tau^\alpha = \mathbf{n}^\alpha \otimes \mathbf{s}^\alpha : \boldsymbol{\sigma}$ is the resolved shear stress (RSS), and g^α is the critical resolved shear stress (CRSS) of the α^{th} slip system. $\dot{\gamma}_0^\alpha = 0.001\ s^{-1}$ and $m_{sl} = 20$ are the reference shear rate and strain rate sensitivity parameter for slip, respectively. The CRSS is given by:

$$g^\alpha = g_0 + \int_0^t \dot{g}^\alpha_{sl-sl} dt + \int_0^t \dot{g}^\alpha_{sl-tw} dt \tag{A-5}$$

Here, g_0 is the initial strength of the slip system. Eq. (1) and Eq. (2) describe g_0 for conventionally manufactured and AM SS316L respectively and is not repeated here for brevity. The second term in Eq. A-5 represents the slip system hardening due to interactions with other slip systems and is given by:

$$\dot{g}^\alpha_{sl-sl} = \frac{\nabla \mu b}{2\sqrt{\rho}} \sum_{\beta=1}^{N_{sl}} \dot{\rho}^\beta \tag{A-6}$$

The rate of evolution of dislocation density is calculated using the Kocks-Mecking expression as [58]:

$$\dot{\rho}^\alpha = \frac{1}{b^\alpha}\left(\frac{1}{l^\alpha} - 2y_c^\alpha \rho^\alpha\right)|\dot{\gamma}^\alpha| \tag{A-7}$$

The first term in equation (A-7) denotes the rate of multiplication of dislocations, which depends on the mean free path l^α. The second term denotes the rate of annihilation of dislocations due to dynamic recovery with y_c^α denoting the annihilation radius. The mean free path for dislocation motion is given by:

$$l^\alpha = \frac{K^\alpha_{mul}}{\sqrt{\sum_{\beta \neq \alpha} \rho^\beta}} \tag{A-8}$$

Here, K^α_{mul} is material parameter characterizing rate of dislocation multiplication and is determined by fitting with experiments. After Kalidindi et al. [59], the hardening of the slip systems due to twinning is taken to arise from the non-coplanar twins acting as barriers to dislocation motion. The strength of this hardening depends on twin spacing, which, in turn, is assumed to be inversely proportional to the twin v.f. Therefore $\dot{g}^\alpha_{sl-tw}$ is given by:

$$\dot{g}^\alpha_{sl-tw} = 0.5 H_{sl-tw} \left(\sum_{\beta=1}^{\beta=N_{tw}^{NCP}} f^\beta\right)^{-0.5} \dot{f}^\beta \tag{A-9}$$

Here, H_{sl-tw} is the hardening coefficient of the hardening of slip systems due to twinning and N_{tw}^{NCP} is the number of non-coplanar twin systems.

A.2 Constitutive equations for twinning

A flow rule similar to slip is adopted for twinning:

$$\dot{\gamma}^\beta = \dot{\gamma}_0^\beta \left|\frac{\tau^\beta}{g^\beta}\right|^{m_{tw}} \tag{A-10}$$

Here, τ^β is the RSS on the leading partial [60], g^β is the CRSS of the β^{th} twin system, respectively, and $\dot{\gamma}_0^\beta$ and m_{tw} are the reference shear rate and strain rate sensitivity parameter for twin, respectively. We compute the rate of increase of the twin v.f. as $\dot{f}^\beta = \frac{\dot{\gamma}^\beta}{\gamma_{tw}}$; where $\gamma_{tw} = \frac{1}{\sqrt{2}}$ is the twinning shear of the FCC crystal. While a similar approach has been taken for twinning in metals of other crystal classes such as HCP Magnesium [61], some key differences exist in the mechanism of twinning in austenitic steels.

In the case of non-cubic materials, strain accrual on the twin systems is non-zero only if the RSS is positive, i.e., twinning is polar. In the case of cubic materials, however, the direction of the RSS affects the twin systems differently. As shown in Table A-1, each slip system corresponds to two partials, and both can serve as the leading partial of a twin system. Figure A-1 schematically shows the partials corresponding to the $(111)[01\bar{1}]$ slip

system. To ascertain which of the two partials should be adopted as the leading partial of the corresponding twin system, we adopted the following strategy. If the RSS of the slip system is positive (see Figure A-1a), then we consider Partial 1 as the leading partial and Partial 2 as the trailing partial. By contrast, if the RSS is negative (see Figure A-1b), we consider the negative of Partial 2 as the leading partial and the negative of Partial 1 as the trailing partial. The CRSS of the twin systems are given by:

$$g^{\beta} = g_0^{\beta} + \int_0^t \left(\dot{g}^{\beta}_{tw-tw} + \dot{g}^{\beta}_{tw-sl}\right) dt \tag{A-11}$$

where g_0^{β} is the intrinsic strength of the twin systems which is given by Byun's formula [35]:

$$g_0^{\beta} = \frac{2\gamma_{eff}^{SFE}}{b^{\beta}} \tag{A-12}$$

Here, $b^{\beta} = \frac{a_0}{\sqrt{6}}$ is the magnitude of the Burgers vector of the partial dislocation and γ_{eff}^{SFE} is the effective stacking fault energy under the applied stress computed as [32,62]:

$$\gamma_{eff}^{SFE} = \gamma_0^{SFE} + \frac{\mathrm{n}^{\beta} \otimes s_T^{\beta} : \sigma - \mathrm{n}^{\beta} \otimes s_L^{\beta} : \sigma}{2} b^{\beta} \tag{A-13}$$

where γ_0^{SFE} is the stacking fault energy at no applied stress, and $\mathrm{n}^{\beta} \otimes s_T^{\beta}$ and $\mathrm{n}^{\beta} \otimes s_L^{\beta}$ are the RSS on the trailing and leading partials, respectively. Therefore, unlike slip, the intrinsic strength of the twin systems is dependent on the current stress levels and the orientation of the partials.

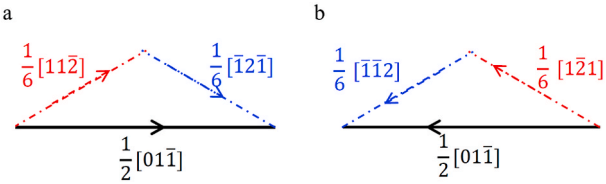

Fig. A.1. Determination of leading and trailing partials from the direction of the RSS. The black arrow denotes the direction of the RSS. The blue and red vectors denote the leading and trailing partials, respectively.

$\dot{g}^{\beta}_{tw-tw}$ in equation (A-11) represents the hardening of the twin systems due to interactions with other twin systems. After Kalidindi et al. [59], it is given as:

$$g^{\alpha}_{tw-tw} = H^{NCP}_{tw-tw}\left(\bar{f}^{\beta}\right)^{p}\left(\sum_{\beta=1}^{\beta=N_{tw}^{NCP}} \dot{\gamma}^{\beta}\right) + H^{CP}_{tw-tw}\left(\bar{f}^{\beta}\right)^{q}\left(\sum_{\beta=1}^{\beta=N_{tw}^{CP}} \dot{\gamma}^{\beta}\right) \tag{A-14}$$

where H^{NCP}_{tw-tw} and p, and H^{CP}_{tw-tw} and q are the hardening parameters for the other non-coplanar and coplanar twin systems, respectively. $\bar{f}^{\beta} = \sum_{\beta=1}^{\beta=N_{tw}} f^{\beta}$ is the total twin v.f., $\dot{g}^{\beta}_{tw-sl}$ represents the hardening of the twin systems due to interactions with other slip systems; after Salem et al. [63], it is given as

$$g^{\alpha}_{tw-sl} = H_{tw-sl}\left(\bar{\gamma}^{\alpha}\right)^{r}\left(\sum_{\alpha=1}^{\alpha=N_{sl}} \dot{\gamma}^{\alpha}\right) \tag{A-15}$$

where H_{tw-sl}, r are the hardening parameters for the twin systems due to slip. $\bar{\gamma}^{\alpha}$ is the total accumulated strain on all slip systems.

A.2.1 Twinning induced lattice reorientation

When the total twin v.f. at a material point ($\bar{f}^{\beta}$) reaches a critical value (f_{cr}), twinning induced lattice reorientation is applied. The rotation matrix $R^{\beta'}$ is given by $R^{\beta'} = -I + 2n^{\beta'} \otimes n^{\beta'}$; here I is the second-order identity tensor and β' is twin system based on which the lattice is rotated. The predominant twin reorientation scheme [64] is used to determine β' wherein the twin system with the highest volume fraction is chosen as β'. Once the lattice reorientation is applied, the RSS of all the slip and twin systems are recalculated for the new orientation. The twin v.f. of all the twin systems is reset to zero; this allows for retwinning and accrual of slip in the reoriented regions.

Kalidindi et al. [59] noted that the number of active slip systems with the twin is expected to be much smaller than the number of active slip systems in the matrix. Therefore, slip within the twin (third term in Eq. A-3) is not considered in this work. It is noteworthy that, due to the reorientation scheme applied, slip within the reoriented regions is possible after lattice reorientation. The crystal plasticity constitutive model described above is implemented as a User Material (UMAT) subroutine in the commercial finite element code ABAQUS. The time integration scheme of Huang et al. [65] is used.

A.3 Model parameters

Table A-2 lists the model parameters used in this work. The source of the parameters obtained by fitting with the experiments of Karaman et al. [32]are indicated as "fitted" and the sources for the other parameters are indicated in the Source column, where applicable.

Table A-2
Material parameters for the SS316L used in this work. All the elastic constants, strength and hardening parameters are in MPa.

Quantity	Value	Source	Equation No.
Elastic constants (MPa)	$C_{11} = 204600$ $C_{44} = 126200$ $C_{12} = 137700$	[66]	–
Shear Modulus (MPa)	$\mu = 74000$	[41]	A-5
Lattice constant (nm)	$a_0 = 0.357$	–	–
Reference shear rate (s^{-1})	$\dot{\gamma}_0^{\alpha} = 0.001$	–	A-4
Strain rate sensitivity parameter	$m_{sl} = 20$	–	A-4
Lattice resistance (MPa)	$g_f = 95$	[41]	1
Lattice resistance (MPa)	$g_f^{AM} = 40$	[39]	2
Dislocation multiplication	$K_{mul}^{\alpha} = 40$	Fitted	A-8
Dislocation multiplication	$y_c^{\alpha} = 3.5\, b^{\alpha}$	Fitted	A-8
Hall-Petch coefficient (MPa $\sqrt{\text{mm}}$)	$k_{HP} = 5.5$	–	A-5
Hardening due to twinning (MPa)	$H_{sl-tw} = 50$	Fitted	A-6
Reference shear rate (s^{-1})	$\dot{\gamma}_0^{\beta} = 0.001$	–	A-9
Strain rate sensitivity parameter	$m_{tw} = 20$	–	A-9
Stacking fault energy (Jm^{-2})	$\gamma_0^{SFE} = 27 \times 10^{-3}$	[67]	A-12
Hardening due to twin (MPa)	$H_{tw-tw}^{NCP} = 200$, p = 0.4 $H_{tw-tw}^{CP} = 450$, q = 1.0	Fitted	A-14
Hardening due to slip (MPa)	$H_{tw-sl} = 250$, r = 0.7	Fitted	A-15
Critical twin v.f.	$f_{cr} = 0.98$	–	–

References

[1] Z. Sun, X. Tan, S.B. Tor, C.K. Chua, Simultaneously enhanced strength and ductility for 3D-printed stainless steel 316L by selective laser melting, NPG Asia Materials 10 (4) (2018) 127–136.
[2] Y.M. Wang, T. Voisin, J.T. McKeown, J. Ye, N.P. Calta, Z. Li, Z. Zeng, Y. Zhang, W. Chen, T.T. Roehling, R.T. Ott, M.K. Santala, Philip J. Depond, M.J. Matthews, A. V. Hamza, T. Zhu, Additively manufactured hierarchical stainless steels with high strength and ductility, Nature Materials 17 (1) (2018) 63–71.
[3] S.-H. Sun, T. Ishimoto, K. Hagihara, Y. Tsutsumi, T. Hanawa, T. Nakano, Excellent mechanical and corrosion properties of austenitic stainless steel with a unique crystallographic lamellar microstructure via selective laser melting, Scripta Mater. 159 (2019) 89–93.
[4] X. Wang, J.A. Muñiz-Lerma, O. Sanchez-Mata, S.E. Atabay, M. Attarian Shandiz, M. Brochu, Single-crystalline-like stainless steel 316L with different geometries fabricated by laser powder bed fusion, Progress in Additive Manufacturing 5 (1) (2020) 41–49.
[5] X. Wang, J.A. Muñiz-Lerma, M. Attarian Shandiz, O. Sanchez-Mata, M. Brochu, Crystallographic-orientation-dependent tensile behaviours of stainless steel 316L fabricated by laser powder bed fusion, Materials Science and Engineering: A 766 (2019) 138395.
[6] Y.-D. Im, K.-H. Kim, K.-H. Jung, Y.-K. Lee, K.-H. Song, Anisotropic mechanical behavior of additive manufactured AISI 316L steel, metallurgical and materials transactions A 50 (4) (2019) 2014–2021.
[7] A. Charmi, R. Falkenberg, L. Ávila, G. Mohr, K. Sommer, A. Ulbricht, M. Sprengel, R. Saliwan Neumann, B. Skrotzki, A. Evans, Mechanical anisotropy of additively manufactured stainless steel 316L: An experimental and numerical study, Materials Science and Engineering: A (2020) 140154.
[8] T. Chen, L. Tan, Z. Lu, H. Xu, The effect of grain orientation on nanoindentation behavior of model austenitic alloy Fe-20Cr-25Ni, Acta Mater. 138 (2017) 83–91.
[9] W. Chen, T. Kitamura, M. Feng, Creep and fatigue behavior of 316L stainless steel at room temperature: experiments and a revisit of a unified viscoplasticity model, Int. J. Fatig. 112 (2018) 70–77.
[10] A. Charmi, R. Falkenberg, L. Ávila, G. Mohr, K. Sommer, A. Ulbricht, M. Sprengel, R. Saliwan Neumann, B. Skrotzki, A. Evans, Mechanical anisotropy of additively manufactured stainless steel 316L: An experimental and numerical study, Materials Science and Engineering: A 799 (2021) 140154.
[11] K.M. Bertsch, G. Meric de Bellefon, B. Kuehl, D.J. Thoma, Origin of dislocation structures in an additively manufactured austenitic stainless steel 316L, Acta Mater. 199 (2020) 19–33.
[12] Y. Hong, C. Zhou, Y. Zheng, L. Zhang, J. Zheng, The cellular boundary with high density of dislocations governed the strengthening mechanism in selective laser melted 316L stainless steel, Materials Science and Engineering: A 799 (2021) 140279.
[13] Z. Li, B. He, Q. Guo, Strengthening and hardening mechanisms of additively manufactured stainless steels: the role of cell sizes, Scripta Mater. 177 (2020) 17–21.
[14] B. Zhou, P. Xu, W. Li, Y. Liang, Y. Liang, Microstructure and anisotropy of the mechanical properties of 316L stainless steel fabricated by selective laser melting, Metals 11 (5) (2021) 775.
[15] T.R. Smith, J.D. Sugar, C. San Marchi, J.M. Schoenung, Strengthening mechanisms in directed energy deposited austenitic stainless steel, Acta Mater. 164 (2019) 728–740.
[16] T. Voisin, J.-B. Forien, A. Perron, S. Aubry, N. Bertin, A. Samanta, A. Baker, Y. M. Wang, New insights on cellular structures strengthening mechanisms and thermal stability of an austenitic stainless steel fabricated by laser powder-bed-fusion, Acta Mater. 203 (2021) 116476.
[17] K.A. Sofinowski, S. Raman, X. Wang, B. Gaskey, M. Seita, Layer-wise engineering of grain orientation (LEGO) in laser powder bed fusion of stainless steel 316L, Additive Manufacturing 38 (2021) 101809.
[18] B.N. Lucas, W.C. Oliver, Indentation power-law creep of high-purity indium, Metallurgical and Materials Transactions A 30 (3) (1999) 601–610.
[19] W.C. Oliver, G.M. Pharr, Measurement of hardness and elastic modulus by instrumented indentation: advances in understanding and refinements to methodology, Journal of Materials Research 19 (1) (2004) 3.
[20] A.E. Giannakopoulos, P.L. Larsson, R. Vestergaard, Analysis of vickers indentation, international journal of solids and structures 31 (19) (1994) 2679–2708.
[21] F.K. Yan, G.Z. Liu, N.R. Tao, K. Lu, Strength and ductility of 316L austenitic stainless steel strengthened by nano-scale twin bundles, Acta Materialia 60 (3) (2012) 1059–1071.
[22] A.K. Agrawal, A. Singh, Limitations on the hardness increase in 316L stainless steel under dynamic plastic deformation, Materials Science and Engineering: A 687 (2017) 306–312.
[23] C. Tromas, J.C. Stinville, C. Templier, P. Villechaise, Hardness and elastic modulus gradients in plasma-nitrided 316L polycrystalline stainless steel investigated by nanoindentation tomography, Acta Materialia 60 (5) (2012) 1965–1973.
[24] W.M. Tucho, V.H. Lysne, H. Austbø, A. Sjolyst-Kverneland, V. Hansen, Investigation of effects of process parameters on microstructure and hardness of SLM manufactured SS316L, J. Alloys Compd. 740 (2018) 910–925.
[25] J.J. Marattukalam, D. Karlsson, V. Pacheco, P. Beran, U. Wiklund, U. Jansson, B. Hjörvarsson, M. Sahlberg, The effect of laser scanning strategies on texture, mechanical properties, and site-specific grain orientation in selective laser melted 316L SS, Mater. Des. 193 (2020) 108852.
[26] S. Gorsse, C. Hutchinson, M. Gouné, R. Banerjee, Additive manufacturing of metals: a brief review of the characteristic microstructures and properties of steels, Ti-6Al-4V and high-entropy alloys, Science and Technology of Advanced Materials 18 (1) (2017) 584–610.
[27] A.J. Birnbaum, J.C. Steuben, E.J. Barrick, A.P. Iliopoulos, J.G. Michopoulos, Intrinsic strain aging, Σ3 boundaries, and origins of cellular substructure in additively manufactured 316L, Additive Manufacturing 29 (2019) 100784.
[28] A.J. Birnbaum, H. Ryou, J.C. Steuben, A.P. Iliopoulos, K.J. Wahl, J.G. Michopoulos, Nested size effects in the nanoindentation response of additively manufactured 316L stainless steel, Mater. Lett. 280 (2020) 128570.
[29] F. Pöhl, C. Hardes, F. Scholz, J. Frenzel, Orientation-dependent deformation behavior of 316L steel manufactured by laser metal deposition and casting under local scratch and indentation load, Materials 13 (7) (2020) 1765.
[30] Y.Z. Xia, H. Bei, Y.F. Gao, D. Catoor, E.P. George, Synthesis, characterization, and nanoindentation response of single crystal Fe–Cr–Ni alloys with FCC and BCC structures, Materials Science and Engineering: A 611 (2014) 177–187.
[31] M. Kato, Hall–Petch Relationship and Dislocation Model For deformation of ultrafine-grained and nanocrystalline metals, MATERIALS TRANSACTIONS 55 (1) (2014) 19–24.
[32] I. Karaman, H. Sehitoglu, H.J. Maier, Y.I. Chumlyakov, Competing mechanisms and modeling of deformation in austenitic stainless steel single crystals with and without nitrogen, Acta Materialia 49 (19) (2001) 3919–3933.

[33] M.S. Pham, B. Dovgyy, P.A. Hooper, Twinning induced plasticity in austenitic stainless steel 316L made by additive manufacturing, Materials Science and Engineering: A 704 (2017) 102–111.
[34] B.C. De Cooman, Y. Estrin, S.K. Kim, Twinning-induced plasticity (TWIP) steels, Acta Mater. 142 (2018) 283–362.
[35] T.S. Byun, On the stress dependence of partial dislocation separation and deformation microstructure in austenitic stainless steels, Acta Materialia 51 (11) (2003) 3063–3071.
[36] Y. Yin, J. Sun, J. Guo, X. Kan, D. Yang, Mechanism of high yield strength and yield ratio of 316 L stainless steel by additive manufacturing, Materials Science and Engineering: A 744 (2019) 773–777.
[37] M. Calcagnotto, D. Ponge, E. Demir, D. Raabe, Orientation gradients and geometrically necessary dislocations in ultrafine grained dual-phase steels studied by 2D and 3D EBSD, Materials Science and Engineering: A 527 (10) (2010) 2738–2746.
[38] S. Gao, Z. Hu, M. Duchamp, P.S.S.R. Krishnan, S. Tekumalla, X. Song, M. Seita, Recrystallization-based grain boundary engineering of 316L stainless steel produced via selective laser melting, Acta Mater. 200 (2020) 366–377.
[39] L. Cui, S. Jiang, J. Xu, R.L. Peng, R.T. Mousavian, J. Moverare, Revealing relationships between microstructure and hardening nature of additively manufactured 316L stainless steel, Mater. Des. 198 (2021) 109385.
[40] X. Wang, J.A. Muñiz-Lerma, O. Sánchez-Mata, M. Attarian Shandiz, M. Brochu, Microstructure and mechanical properties of stainless steel 316L vertical struts manufactured by laser powder bed fusion process, Materials Science and Engineering: A 736 (2018) 27–40.
[41] M. Shamsujjoha, S.R. Agnew, J.M. Fitz-Gerald, W.R. Moore, T.A. Newman, High strength and ductility of additively manufactured 316L stainless steel explained, metallurgical and materials transactions A 49 (7) (2018) 3011–3027.
[42] G. Monnet, M.A. Pouchon, Determination of the critical resolved shear stress and the friction stress in austenitic stainless steels by compression of pillars extracted from single grains, Mater. Lett. 98 (2013) 128–130.
[43] B. He, B. Hu, H. Yen, G. Cheng, Z. Wang, H. Luo, M. Huang, High dislocation density–induced large ductility in deformed and partitioned steels, Science 357 (6355) (2017) 1029–1032.
[44] S. Ghorbanpour, M. Zecevic, A. Kumar, M. Jahedi, J. Bicknell, L. Jorgensen, I. J. Beyerlein, M. Knezevic, A crystal plasticity model incorporating the effects of precipitates in superalloys: application to tensile, compressive, and cyclic deformation of Inconel 718, Int. J. Plast. 99 (2017) 162–185.
[45] I. Karaman, H. Sehitoglu, K. Gall, Y.I. Chumlyakov, H.J. Maier, Deformation of single crystal Hadfield steel by twinning and slip, Acta Materialia 48 (6) (2000) 1345–1359.
[46] W.D. Nix, H. Gao, Indentation size effects in crystalline materials: a law for strain gradient plasticity, Journal of the Mechanics and Physics of Solids 46 (3) (1998) 411–425.
[47] K. Singh, S. Sangal, G. Murty, Hall–Petch behaviour of 316L austenitic stainless steel at room temperature, Materials science and technology 18 (2) (2002) 165–172.
[48] B. Kashyap, K. Tangri, On the Hall-Petch relationship and substructural evolution in type 316L stainless steel, Acta metallurgica et materialia 43 (11) (1995) 3971–3981.
[49] Z. Yanushkevich, S. Dobatkin, A. Belyakov, R. Kaibyshev, Hall-Petch relationship for austenitic stainless steels processed by large strain warm rolling, Acta Mater. 136 (2017) 39–48.
[50] J.W. Gahn, Hardening by spinodal decomposition, Acta Metallurgica 11 (12) (1963) 1275–1282.
[51] M.R. Staker, D.L. Holt, The dislocation cell size and dislocation density in copper deformed at temperatures between 25 and 700°C, Acta Metallurgica 20 (4) (1972) 569–579.
[52] K. Saeidi, X. Gao, Y. Zhong, Z.J. Shen, Hardened austenite steel with columnar sub-grain structure formed by laser melting, Materials Science and Engineering: A 625 (2015) 221–229.
[53] D. Peirce, R.J. Asaro, A. Needleman, Material rate dependence and localized deformation in crystalline solids, Acta Metallurgica 31 (12) (1983) 1951–1976.
[54] R.J. Asaro, Micromechanics of Crystals and Polycrystals, in: J.W. Hutchinson, T. Y. Wu (Eds.), Advances in Applied Mechanics, Elsevier, 1983, pp. 1–115.
[55] S.R. Kalidindi, Incorporation of deformation twinning in crystal plasticity models, Journal of the Mechanics and Physics of Solids 46 (2) (1998) 267–290.
[56] R.J. Asaro, J.R. Rice, Strain localization in ductile single crystals, journal of the mechanics and physics of solids 25 (5) (1977) 309–338.
[57] J.W. Hutchinson, Bounds and self-consistent estimates for creep of polycrystalline materials, proceedings of the royal society of london, A. Mathematical and physical sciences 348 (1652) (1976) 101–127.
[58] U.F. Kocks, H. Mecking, Physics and phenomenology of strain hardening: the FCC case, Progress in Materials Science 48 (3) (2003) 171–273.
[59] S.R. Kalidindi, Modeling anisotropic strain hardening and deformation textures in low stacking fault energy fcc metals, International Journal of Plasticity 17 (6) (2001) 837–860.
[60] I. Gutierrez-Urrutia, S. Zaefferer, D. Raabe, The effect of grain size and grain orientation on deformation twinning in a Fe–22wt.% Mn–0.6wt.% C TWIP steel, Materials Science and Engineering: A 527 (15) (2010) 3552–3560.
[61] J. Zhang, S.P. Joshi, Phenomenological crystal plasticity modeling and detailed micromechanical investigations of pure magnesium, Journal of the Mechanics and Physics of Solids 60 (5) (2012) 945–972.
[62] I. Karaman, H. Sehitoglu, K. Gall, Y.I. Chumlyakov, On the deformation mechanisms in single crystal hadfield manganese steels, Scripta Materialia 38 (6) (1998) 1009–1015.
[63] A.A. Salem, S.R. Kalidindi, S.L. Semiatin, Strain hardening due to deformation twinning in α-titanium: constitutive relations and crystal-plasticity modeling, Acta Materialia 53 (12) (2005) 3495–3502.
[64] C.N. Tomé, R.A. Lebensohn, U.F. Kocks, A model for texture development dominated by deformation twinning: application to zirconium alloys, Acta Metallurgica et Materialia 39 (11) (1991) 2667–2680.
[65] Y. Huang, A User-Material Subroutine Incroporating Single Crystal Plasticity in the ABAQUS Finite Element Program, Harvard Univ. Cambridge, 1991.
[66] B. Clausen, T. Lorentzen, T. Leffers, Self-consistent modelling of the plastic deformation of f.c.c. polycrystals and its implications for diffraction measurements of internal stresses, Acta Materialia 46 (9) (1998) 3087–3098.
[67] G. Meric de Bellefon, J.C. van Duysen, K. Sridharan, Composition-dependence of stacking fault energy in austenitic stainless steels through linear regression with random intercepts, J. Nucl. Mater. 492 (2017) 227–230.
[68] Yong Chen Yeoh, et al., Matteo Seita, Multiscale microstructural heterogeneity and mechanical property scatter in Inconel 718 produced by directed energy deposition, Journal of Alloys and Compounds 887 (2021) 161426, https://doi.org/10.1016/j.jallcom.2021.161426. In press.